3. MICROSTRUCTURAL AND GEOMECHANICAL CONSTRAINTS ON FLUID FLOW AT THE COSTA RICA CONVERGENT MARGIN, OCEAN DRILLING PROGRAM LEG 170[1]

Alistair J. Bolton,[2,3] Paola Vannucchi,[4] M. Ben Clennell,[5] and Alex Maltman[2]

ABSTRACT

We present the results of detailed mesoscopic and microscopic observations made on sediments obtained from Sites 1040 and 1043, located at the toe of the Costa Rica convergent margin. Inferences drawn on the evolution of deformation microstructures, and in particular the role of fluids on their formation, were supplemented by geotechnical hydrogeological laboratory tests that elucidated the varying manner with which different sediments deformed both mechanically and hydrologically. Three different structural/hydrological regimes have been identified. The sedimentary prism records episodes of tectonic bulk strain in which fluid pressures fluctuate to form deformation zones of varying orientation. Shear is dominantly compactive, resulting in loss of porosity and subsequent reduction in permeability. These zones are not conducive to forming conduits, even at low effective stresses. The décollement is characterized by more brittle faulting, associated with transient periods of dilation. Such microfabrics can efficiently duct fluids along a fluid-pressure controlled fracture permeability, with an associated rise in permeability at effective stresses approaching near lithostatic in magnitude. In contrast, the underthrust section is dominantly undeformed. Deformation-induced dewatering occurs primarily in the upper lower permeability section. The results have a broad application to structural and hydrological observations made at many other

convergent margins where hydromechanical coupling is intimately related.

INTRODUCTION

Deep-sea drilling by the Ocean Drilling Program (ODP) of several active convergent margins in the last two decades has increased the level of understanding of how such geologically active regions evolve, for example Barbados, Legs 110 and 156 (Mascle, Moore, et al., 1988; Shipley, Ogawa, Blum, et al., 1995) and 171A (Moore, Klaus, et al., 1998); Nankai, Leg 131 (Taira, Hill, Firth, et al., 1991); Peru, Leg 141 (Behrmann, Lewis, Musgrave, et al., 1992); Cascadia, Leg 146 (Westbrook, Carson, Musgrave, et al., 1994; and, more recently, Costa Rica, Leg 170 (Kimura, Silver, Blum, et al., 1997). Highly saturated, weakly bonded sediments respond to tectonic compression by loss of porosity (Bray and Karig, 1985), with subsequent release of large quantities of fluid. The resultant fluid flow can be responsible for the transport of chemically exotic fluids into oceanic waters and may exert a significant control on biological and geochemical fluxes in the oceans (Kastner et al., 1991).

Of particular importance to structural studies are processes occurring within the décollement, where fluids exist at near lithostatic pressures (e.g., Bangs et al., 1990; Moore et al., 1995; Screaton et al., 1995; Fisher et al., 1996). Reduced effective stress along the décollement facilitates decoupling between overriding prism sediments and underthrust material (Housen et al., 1996), in a similar manner to that proposed for the formation of ancient fold and thrust belts (Hubbert and Ruby, 1959). The coexistence of extensive overpressure, implying retarded fluid flow, with sites of accelerated fluid flow represents a paradox and has been modeled as transient episodes of fluid flow (Bekins et al., 1995) superimposed on intervals of retarded flow and pressure buildup (Carson and Screaton, 1998).

Weak sediments deform in a variety of ways, and often the resultant microfabrics provide clues to the behavior of fluids during deformation. This paper describes observations made on sediments retrieved during ODP Leg 170 drilling of the Costa Rica convergent margin. Inferences drawn from structural relationships were augmented by laboratory permeability and deformational experiments, which were designed to examine the extent to which the fluid transmissibility of different microfabrics responds to fluctuations in fluid pressure. Quantitative assessment of structures and qualitative analysis of sediment hydrology provide a sound foundation for further work, such as geochemical interpretation and theoretical flow modeling. Leg 170 drilling of the Costa Rica margin retrieved good quality cores and successfully penetrated the décollement, providing excellent opportunity for expanding understanding of the processes associated with plate convergence, where a comparison can be made with more extensively studied margins such as North Barbados Ridge (Mascle, Moore, et al., 1988; Shipley, Ogawa, Blum, et al., 1995).

Geological Setting of the Costa Rica Margin

Subduction of the Cocos plate beneath the Caribbean plate gives rise to the Costa Rica convergent margin. Plate convergence is at a rate of approximately 8–9 cm/yr (Demets et al., 1990) and in a direction approximately perpendicular to the Middle America Trench. On the sub-

ducting plate, Pliocene–Pleistocene claystones and silty claystones overlie siliceous nannofossil chalk and calcareous diatomites. The absence of trench deposits makes the margin ideal for studies concerning both compactional behavior of unlithified sediments during underthrusting and mass balance and recycling calculations. One of the primary objectives of the leg was to assess the extent to which sediments have been accreted to the continental margin, the mechanisms by which sediments reacted to convergence, and the associated flux of fluids within the area.

Five sites were drilled during Leg 170 (Fig. F1): one reference site on the subducting Cocos plate (Site 1039); two sites through the lower toe slope sediments (henceforth referred to as the sedimentary prism); the décollement, the underthrust section, and oceanic crust (Sites 1040 and Site 1043); and two sites midslope (Sites 1041 and 1042). Here we focus on structures and fluid flow within the toe of the sedimentary prism (Sites 1040 and 1043), allowing comparisons between the underthrust region of these two sites with the stratigraphically equivalent reference site.

Below, the paper consists of five sections. The first section introduces the experimental methodology used for conducting the permeability tests and observing the microstructures. The second section presents the results of this microstructural examination. Where appropriate, different structures are interpreted with regard to fluid behavior during deformation. Subdivisions are made depending on the specific locality where the sediments were retrieved. The third section presents the results of permeability testing. Observed hydrological behavior is correlated with the inferences drawn from microstructural examination. The fourth section amalgamates the results in a model that may explain the observed patterns of fluid flow and deformation. Finally, the fifth section concludes with the pertinent observations.
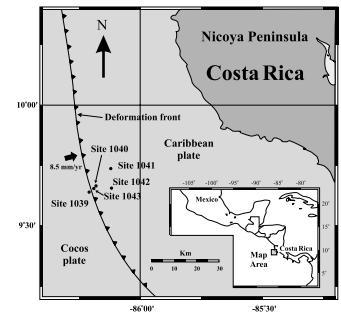
METHODOLOGY

Structural Analysis

Mesoscopic analysis of split-core features were described shipboard (Kimura, Silver, Blum, et al., 1997). Key horizons were identified and samples were extracted for postcruise analysis. Material was impregnated with low-viscosity epoxy resin and ground down into slides for optical microscopic examination. Oriented sediment chips were slowly air-dried before being mounted on metallic stubs and sputter-coated with gold for scanning electronic examination operating in secondary mode.

Permeability and Geomechanical Analysis

Whole-round samples were taken at key intervals from both the reference site and the two prism toe sites. Permeability tests were conducted on cylindrical samples using the constant-rate-of-flow permeameter (Olson and Daniel, 1981) at various values of effective stress before and after shear (Fig. F2). Precise effective stress conditions were achieved by fluctuating the confining pressure and/or the back pressure. The back pressure required to eliminate any air held within the sample was consistently greater than 300 kPa in magnitude. Samples were placed in a flexible, impermeable membrane and housed in a

F1. Leg 170 drilling sites, p. 16.

F2. Experimental setup for permeability/geotechnical analysis, p. 17.

A.J. Bolton et al.
Microstructural and Geomechanical Constraints on Fluid Flow

4
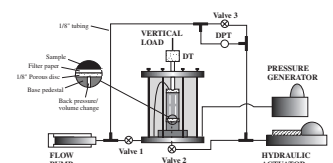
triaxial cell. Fluid was infused into the sample at a constant, predetermined rate, creating a hydraulic gradient and promoting fluid flow along the axis of the cylinder. The associated differential pressure was measured using a differential pressure transducer accurate to ±1 kPa. Permeability is calculated using Darcy's law at steady state, occurring when a constant volume of fluid entering and exiting the sample is coupled with a steady differential pressure. Flow rate was controlled such that differential pressure across the sample did not exceed 100 kPa, equating to a flow rate of approximately 0.5 mL/min for these low-permeability materials. Samples were deformed axially at a constant rate of strain (10^{-5} to 10^{-8} s^{-1}), and axial stress was continuously monitored to beyond failure (5%–30% axial strain depending on the strength of the individual sample). Where the initial permeabilities were high enough (>10^{-17} m^2), fluid was infused through the sample simultaneously with deformation. Comparing the infused fluid volume with the volume of fluid exiting the sample provided information on volumetric changes induced by shear. For example, an increase in sample volume was identified when the volume of permeant entering the sample exceeded the volume of fluid exiting the sample. This volumetric behavior, when coupled with the differential response, allowed calculation of the active permeability change during deformation (the "dynamic permeability" of Stephenson et al., 1994). Where initial permeabilities were low (<10^{-17} m^2), the sample was sheared undrained by closing the base tap of the triaxial cell, hence preventing any pore water drainage to occur. In this instance, no fluid was infused into the sample, and the differential pressure fluctuations could be directly related to deformation-induced fluid pressure changes.

After cessation of shear, the static permeability was measured at different values of effective stress. Comparison of the permeability behavior after shear with that measured under the same conditions before deformation allowed direct assessment of the influence deformation microfabrics exerted on sediment permeability.

MACRO- AND MICROSTRUCTURAL RESULTS

Sedimentary Prism

Core-Scale Observations

Sites 1040 and 1043 penetrated the prism, décollement, and underthrust unit, recovering 371.2 and 150.57 m of core, respectively (Fig. F3). The recovered material is similar at both sites, comprising claystone and silty claystone (Kimura, Silver, Blum, et al., 1997). Deformation within the prism is indicated by a wide range of structures, distinguished both by their morphology and relative distribution throughout the prism. Inclined bedding, microfaults with small (0.5 to 1 cm) offsets, and fracture networks are widely distributed throughout the prism. Fissility, closely spaced fracture networks, brittle-ductile stratal disruption, deformation bands, and incipient scaly fabric tend to be concentrated within certain horizons (terminology used is consistent with definitions within Maltman, 1998). Fluid conduits inferred from geochemical anomalies that may indicate shear zones (Kimura, Silver, Blum, et al., 1997) and structural discontinuities identified from paleontological age reversals are not always coincidental with mesoscopic features. The lower boundary of the prism (i.e., the top of the dé-

F3. Generalized stratigraphic column for three sites, p. 18.
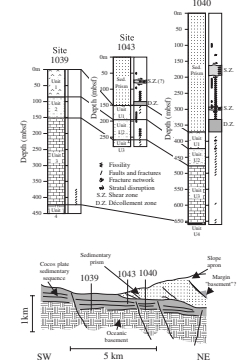
collement zone) is arbitrarily placed at the first occurrence of fractures with polished surfaces, typical of incipient scaly fabric.

Microscopic Observations

Scanning electronic microscopic (SEM) and optical observations on undeformed sections within the prism show that the uppermost 80 m of the section consists of high-porosity sediment with only a weak preferred orientation of clay minerals. Below this depth, clay minerals show increasing levels of particle alignment. Given that depth is the only variable in these relatively homogeneous sediments (only thin lenses of more silt-rich horizons were encountered), clay orientation has arisen primarily in response to gravity induced compaction. Core-based physical properties and logging while drilling (LWD) porosity and bulk density measurements show a gradual decrease in porosity from ~65% to 55% and are in good agreement with microscopic observations. Similar porosity/depth trends have been observed at other convergent margins, such as Cascadia (Westbrook, Carson, Musgrave, et al., 1994).

Deformed horizons are characterized by three principal modes of deformation: kink bands, deformation bands, and small, discrete faults. Kink bands sharply deflect the primary sedimentary fabric. Deformation bands is a general term used to describe planar zones with an appreciable thickness where clay minerals are approximately parallel to the edges of the deformed zone. Although appearing brittle at the macroscopic scale, they maintain a distinctly ductile appearance at the electron-microscopic scale. Faults have a similar appearance to deformation bands but tend to be more localized and brittle, with well defined offsets even at the hand-specimen scale.

The relative timing of each type of deformation structure can be ascertained by crosscutting relationships. Kink bands are the earliest structures formed but are neither abundant nor well developed. They are indiscernible at the macroscopic scale and microscopically occur only at depths greater than 150 meters below seafloor (mbsf). In addition, they tend to localize at high angles (between 40° and 70°) (Fig. F4) to regions where a strong compaction fabric has developed. External kink-band measurements are relatively high (40° to 55°), with internal angles between 40° and 50°. The kink band morphologies at this margin are similar to those observed in the Nankai prism (Suppe, 1985; Byrne et al., 1993) and are indicative of progressive porosity loss through consolidation. The fact that they do not form until at least 150 mbsf suggests that overburden pressure must exceed a critical value before they can nucleate and grow.

Deformation bands displace kink bands and thus were formed at a later stage. They represent the most common features observed in the entire prism, particularly at Site 1040. The length and width of deformation bands vary but do not exceed 5 cm and 2 mm, respectively. Internal structures of the deformation bands are ubiquitously characterized by clay mineral alignment parallel to the shear-zone wall. The overall geometry of the deformation bands varies from numerous networks of bands to singular, thick shear zones (Fig. F5). Where deformation bands form parallel to bedding, they tend to be thicker (0.1 mm) and longer (1 cm) than where they crosscut obliquely to bedding fabric. crosscutting relationships within individual deformation bands suggests that increased levels of strain occur through progressive thickening of individual zones. Below 200 mbsf, zones of deformation bands
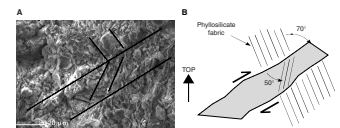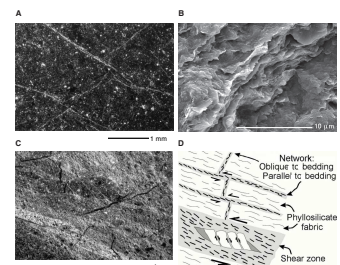
are so numerous that the sediment has two clay mineral orientations, one due to the compaction fabric and the other due to the shear zones. The intense grain alignment has reduced the porosity relative to surrounding, undeformed sediment, suggesting that the overall mode of deformation was compactional in nature. Reverse kink bands and oblique deformation bands may result from rotation of the principal stress component from vertical at the reference site to subhorizontal within the prism.

In contrast to the deformation bands, faults are narrow, discrete discontinuities that are dark red in color (Fig. F6). They crosscut both kink bands and deformation bands and are dominantly 0.01 mm wide and <1 cm in length. Faults are commonly oriented at a high angle to the preferred clay mineral orientation and show a wide spectrum of dihedral angles. SEM observations show that the fault planes are frequently polished and lineated. X-ray energy dispersive spectroscopy analyses on the fault surface do not record any chemical differences between the fault and surrounding sediments that can explain the difference in color, although the technique is not sensitive to any changes in the oxidation state of elements (e.g., Fe). Two shear zones at Site 1040 did contain authigenic barite crystals that, like Barbados (Labaume et al., 1997) are thought to be indicative of fluid flow.

Décollement Zone

Core-Scale Observations

Structural features observed within extracted cores were found to coincide well with geochemical, physical properties, and micropaleontological data, constraining the décollement within a well-defined zone of 38.6 m thickness at Site 1040 and 9 m at Site 1043. Mesoscopic observations reveal a heterogeneous distribution of brittle and ductile deformation features, which grade from a more brittle upper part to a ductile lower part (Fig. F7). At Site 1040, the brittle domain is 24.2 m thick and occupies 63% of the entire décollement thickness.

In the brittle domain, fracture networks disseminate the cores into lenticular, blocky fragments on the millimeter to centimeter scale. Anastomosing, discontinuous, and interpenetrative fractures represent the most disrupted sediments. Some fracture surfaces are polished, and a few, thin horizons of incipient scaly fabric have been recovered. Several millimeter-scale veinlets filled with calcite and rhodocrosite also were recovered.

The ductile domain consists of plastic, silty clay that has suffered intense drilling disturbance, which precludes structural interpretation.

Microscopic Observations

SEM observations from within the brittle domain of the décollement indicate a high level of heterogeneity in the grain size of the sediments, in the deformation style and the clay mineral fabric (Fig. F8). Siltier zones are arranged in laminae or lenses surrounded by clayey material that have experienced sporadic incipient cementation and smectite authigenesis. More clay-rich domains are characterized by poorly oriented smectite with incipient carbonate cementation interspersed with areas of well-developed preferred orientation.

Although the brittle part of the décollement maintains a similar appearance with increasing depth, there is an increase in intensity of frac-
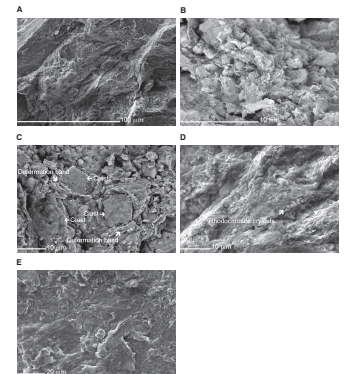

F6. Burrow displaced by inclined faults, p. 21.
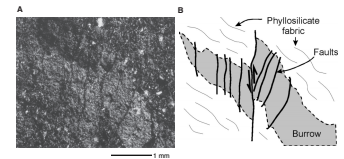
F7. Photo of décollement interval, p. 22.
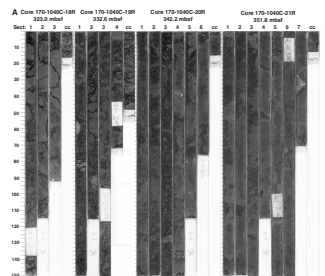
F8. Relevant features of the décollement, p. 24.

tured sediment toward the lower part of the décollement. Deformation is constrained to more clay-rich horizons as irregular anastomosing bands, whereas adjacent areas remain undeformed, indicating extreme strain localization. Incipient scaly fabrics are formed in more clay rich lithologies that are slightly cemented and are characterized by lineated surfaces with some or no polishing. Small aggregates of rhodocrosite crystals also are present in carbonate-poor regions, testifying to fluid flow.

Underthrust Section

Core-Scale Observations

Given the minor amounts of accretion, the underthrust section at both Sites 1040 and 1043 represents the same stratigraphic sequence examined at Site 1039. Clayey diatomites (Unit U1, mid- to late Pleistocene in age) overlie silty claystones (Unit U2, late Miocene to mid-Pleistocene in age), which in turn overlie nannofossil-rich chalks (Unit U3, middle to late Miocene in age). The base of the sequence is marked by a pyroxene gabbro, which contains a K/Ar datum of approximately 15 m.y. (J. Griffin, pers. comm., 1998).

Underthrusting results in a progressive increase in overburden pressure as the overlying wedge thickens. The response of each unit to burial can therefore be quantified by comparing the respective physical properties at each site. For instance, at Site 1040, Unit U1 records a volume loss of 34.73%, Unit U2 has suffered 14.66% volume loss, and Unit U3, 58.92% (Fig. F3) (Kimura, Silver, Blum, et al., 1997). The deformation style shows an abrupt change between the bottom of the décollement and the upper part of the underthrust unit. The plastically deformed lower section of the décollement is replaced by largely undeformed to occasionally brittle deformed sediments in which primary sedimentary fabrics such as burrows are well preserved. The faults are morphologically different from within the prism, displaying discrete, narrow displacements with no ductile component. Where offsets can be discerned, they commonly show a reverse sense of displacement and may form from partitioning of the compressive stress component prevalent in the prism and décollement into the upper part of the underthrust section. With increasing depth, the number of faults decreases and shows geometries similar to those faults observed at the reference site. If the dominant stress orientation at the reference site is vertical, then extensional structures seen both at Site 1039 and within underthrust sediments attest to early differential compaction and may indicate structures arising from the initial flexure of the oceanic crust as it enters the subduction zone. Furthermore, the décollement represents a major structural discontinuity that divides dominantly contractional deformation features above in the prism (implying near horizontal principal stress) to vertical stress within the underlying underthrust units. Such efficient decoupling has been noted at other margins from palaeomagnetic measurements (Housen et al., 1996). Deformation becomes more intense in the vicinity of the gabbro intrusion encountered at the base of Site 1040, where layer-parallel extension structures such as pinch and swell and boudinage occur.

A.J. Bolton et al.
Microstructural and Geomechanical Constraints on Fluid Flow

8

Microscopic Observations

Compaction within the upper part of Unit U1 is largely taken up by draping of clay minerals around more rigid silty grains. Porosity loss occurs primarily by reorientation and more intensely aligned grains than seen in equivalent horizons at the reference site. Occasional layers show anastomosing and discrete deformation bands that contain silt grains oriented parallel to the band edges. The lower part of Unit U1 contains undeformed pyrite-filled fractures and framboids.

Unit U2 is markedly less deformed than unit U1 but contains sporadic well developed faults. U2 faults can reach several centimeters in length and are detectable mesoscopically. They are characterized by strong clay orientation and lineated surfaces. The intensity of deformation fabrics increases with depth, where occasional fracturing of microfossils can be observed. The majority of Unit U3 is undeformed, in contrast to the vicinity of the gabbroic intrusion, where porosity is markedly lower and all mineral grains are intensely aligned.

Quartz and silica recrystallization occurs sporadically throughout the underthrust section (Fig. F9) but shows no prevalence for particular horizons. At Site 1039, recrystallization occurs at 375.94 mbsf, in contrast to Site 1040, where no recrystallization was observed above 411.7 mbsf. Silty grains are commonly surrounded by calcite, which can form a patchy, incipient cementation.

PERMEABILITY AND MECHANICAL OBSERVATIONS

The relationship between permeability and effective stress prior to deformation is shown in Figure F10A. The gradient of each line indicates the level of stress dependence of permeability, and it can be observed that increasing the mean effective stress from 175 kPa to a maximum of 1200 kPa leads to a decrease in permeability of approximately half an order of magnitude in most cases. This permeability reduction corresponds to a porosity loss of only several porosity units (Fig. F10B). Given the limitations of the test equipment (maximum stresses of approximately 1.6 MPa are achievable), all samples tested are overconsolidated with respect to the in situ effective stress acting upon the sediment. Any porosity loss due to loading therefore represents the elastic portion of a typical consolidation curve and may explain the relatively small change in both porosity and permeability with increasing effective stress.

The range of permeabilities measured before, during, and after shear are summarized in Figure F11. Permeability evolution during shear in all cases bar one displays small-scale changes in permeability (less than one order of magnitude). Similarly, in the majority of cases, the permeability for a given effective stress after shear did not differ significantly from the equivalent preshear permeability. In other words, deformation predominantly has little effect on the overall permeability of the material, even when effective stresses approach zero magnitude (in other words at extreme levels of overpressure).

The sample that showed the greatest variation in permeability was a stiff, friable intensely overconsolidated claystone (Sample 170-1040C-13R-5, 88–105 cm). This sample, although extracted from within the prism, contained intact fabrics that typically characterized the upper part of the décollement. Geochemical and physical properties varia-
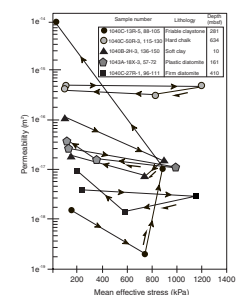
F9. Evidence for recrystallization, p. 25.
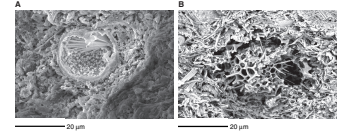
F10. Permeability and porosity vs. effective stress, p. 26.
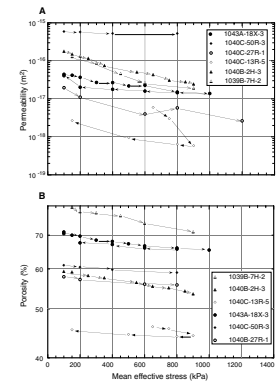
F11. Permeability vs. effective stress relationships, p. 27.

tions (Kimura, Silver, Blum, et al., 1997) confirm that this interval represents a fault zone acting as an efficient conduit for fluid flow. In this instance, axial deformation induced a markedly different fluid pressure response and permeability change than observed in any of the other samples. Whereas compactive shear, typical of the majority of these sediments, induced both increases in fluid pressure and bulk decreases in permeability, shearing of this heavily overconsolidated sediment induced a rapid drop in fluid pressure (Fig. F12A), consistent with mechanical principles of dilation in overconsolidated sediments (Karig, 1990). Although porosity varied by little more than 6% (from 44% at the highest levels of effective stress before shear to 49.4% at low effective stress after shear), the permeability of the sample increased by almost four orders of magnitude. Furthermore, specimen failure was intensely localized and brittle and induced a permeability increase from 3×10^{-18} m^2 to 1×10^{-15} m^2 (Fig. F12C) directly before and after shear. Increased effective stress after failure induces permeability reduction, which may reflect the closure of newly formed dilant fractures. The permeability of this sample therefore ranges by nearly four orders of magnitude through the whole stress-strain path, from 6×10^{-19} m^2 before shear (900 kPa effective stress) to 2×10^{-15} m^2 after shear (50 kPa effective stress).

Hydrological Discussion

It was observed in the majority of cases that deformation had an insignificant effect on the permeability of these samples (summarized in Fig. F11). Even though all samples were tested in an overconsolidated state (due to equipment limitations), they gradually consolidated during shear in a diffuse manner. We infer that significant permeability variations do not occur in the absence of any significant microfabrics.

Two samples that deformed in a predominantly brittle manner (Samples 170-1040C-50R-3, 115–130 cm, and 13R-5, 88–105 cm) were notably more indurated, and yet displayed individually vastly different hydrological response during and after shear. The overconsolidated chalk (Sample 170-1040C-50R-3) contained a relatively high initial permeability, which displayed very little permeability reduction before, during, or after shear even though the material failed along single plane with a well-defined peak stress. In other words, brittle failure has little influence on hydrological properties when the initial permeability is high, even at low effective stresses. In contrast, the permeability of the friable claystone increased by nearly four orders of magnitude when both brittle fractures formed and fluid pressures were raised. Postshear permeability was more sensitive to changes in effective stress than porosity variations, which may reflect the opening and closure of fractures in response to fluid pressure fluctuations (and hence effective stress) that allows increased interconnectivity and fluid flow. Fracture closure results in fluid flow that is controlled by matrix properties (e.g., porosity) as opposed to stress. Similar permeability behavior has been observed in situ within the Barbados décollement (Fisher et al., 1996; Screaton et al., 1997) and during laboratory tests (Brown, 1995; Zwart et al., 1997) on various sediments from different margins.

F12. Differential fluid pressure vs. time, porosity vs. permeability, and permeability vs. effective stress, p. 28.
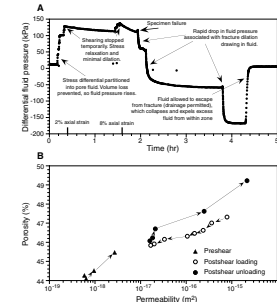
# KINEMATIC EVOLUTION
OF DEFORMATION STRUCTURES

By observing the interrelationships of different structures, their internal characteristics (e.g., porosity contrast of deformed zones and adjacent undeformed sediment), and permeability behavior during laboratory deformation, it is possible to constrain the timing, the role of fluid pressure, and principal stress orientation within the prism, the décollement, and the underthrust unit.

Sedimentary Prism Deformation

Kink bands display both extensional and compressional offsets and may be both gravitational and tectonic in origin. There is no marked porosity difference within the kink bands and adjacent, undeformed sediment (as revealed by SEM observation) and displacements are small (1–2 mm), indicative of very minor finite strains along discrete discontinuities (Fig. F13).

Deformation bands offset kink bands and contain collapsed porosity. The close association with kink bands and relative crosscutting relationships suggests they formed by progressive strain and grain reorientation from deflected kink-band boundaries, and subsequent densification within the band. The bimodal orientation is feasibly a result of timing and extent of fluid pressure variations during shear (Fig. F13). Such volumetric behavior typifies normally consolidated sediment, and deformation bands oriented obliquely to the primary (consolidation) fabric may form in response to translation of horizontal principal stresses in the sedimentary pile. Laboratory tests (in particular Samples 170-1040B-2H-3, 136–150 cm, and 170-1040C-27R-1, 96–111 cm) consolidated during shear, accompanied by decreasing permeability both during and after shear. If this behavior is representative of natural processes, it can be inferred that such fabrics within the prism would not play a significant role in bulk prism hydrology. However, given that little overpressure exists within the prism, the fluid expulsion necessitated by porosity collapse of the deformation bands has been sufficiently transmitted out of the prism at some point in the structural history. Bedding-parallel deformation bands contain intensely aligned particles, constrained to extremely narrow horizons and are more representative of slip-under conditions of reduced effective stress. The geometries displayed here share similar characteristics to experimental structures of sheared overconsolidated sediment (Skempton, 1966). Typically, a dilating shear zone creates a zone of weakness that allows strain softening to occur within a deformation band, allowing large shear strains to develop within narrow discontinuities. The accompanying hydrological response may be a drop in fluid pressure (Bolton et al., 1999) or a concomitant increase in permeability (Stephenson et al., 1994; Bolton et al., 1998). Transient dilation during shear induces only small increases in permeability before ultimate porosity collapse yields a more permanent decrease in permeability both parallel and perpendicular to the shear zone (Brown et al., 1994). Although the actively deforming sediment may have contributed to sediment dewatering during formation of the shear zones, ultimate porosity collapse reduces the flow capacity. Shear deformation within the prism is therefore unlikely to significantly affect the bulk hydrology.

F13. Formation of kink bands and deformational bands, p. 30.
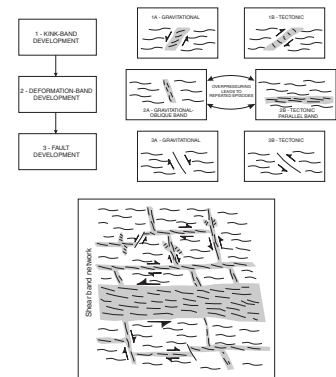
Décollement Deformation

The dewatering and deformational history of the décollement appears less systematic than the prism. Microstructure associations suggest the variable presence of high-porosity zones and low-porosity zones (Fig. F14). Lower porosity regions are both clay rich and silt rich where cementation has occurred. Deformation appears constrained to clay-rich domains, and although porosity has collapsed, calcite and rhodocrosite precipitates within the shear zones suggest focused flow at some point in the structural history. Geochemical observations show that the upper, more brittle portion of the décollement is the principal focus of flow.

Given that the layer-parallel fracture networks transect extremely indurated and, presumably, intensely overconsolidated sediment, we can extrapolate our deformation experiments to processes occurring within the décollement. It has been documented (Fig. F12A) that localized, brittle failure can result in both fluid pressure decrease and a permeability increase of nearly four orders of magnitude with fluctuating fluid pressure (Fig. F12C). The resultant fracture flow is manifest as intervals of fluid pressure build up and shear, until failure and increased interconnectivity of the fractures allows the release of pressurized fluids. At low fluid pressures, flow is matrix dominated and of low permeability, switching to fracture flow and high permeability as the fluid pressure is raised. The mechanism relies upon connectivity between areas of different hydraulic potential that allow fluid circulation into more permeable horizons.

The presence of authigenic minerals within the lower, more ductile part of the décollement indicates that some fluid flow has also occurred within this interval, although the lack of discrete fabrics suggests that this flow is likely to be matrix dominated and therefore would not display the same variation of permeability with effective stress.

Underthrust Section Deformation

Although less numerous, deformation bands with morphologies comparable to those observed within the prism are present in the underthrust section. They maintain an appearance similar to the spaced foliation (Fig. F15) found near scaly fabric zones in the Barbados accretionary prism (Labaume et al., 1997), and to those formed in laboratory experiments (Maltman, pp. 426–429 in Borradaile et al., 1982). The bands are regularly spaced and constrained to certain intervals and have geometries similar to mud-filled veins found at the Peru margin (Brothers et al., 1996).

Other structures, normal faults in particular, are observed throughout the entire underthrust unit. Their prevalence in the upper Unit U1, which has undergone the most significant compaction, suggests that differential compaction is one operative mechanism of unit thinning. The fact that many of the fault surfaces are planar suggests that they have formed solely in response to loading by the overlying prism, rather than in response to flexure of the oceanic plate, where subsequent loading would result in compacted, curviplanar fault surfaces. We are precluded from possible interpretation of the consolidation behavior of the underthrust sediments from laboratory testing, as stresses achievable by the experimental apparatus were not of sufficient magnitude to exceed the maximum in situ consolidation stress.

F14. Microstructures observed within the décollement, p. 31.
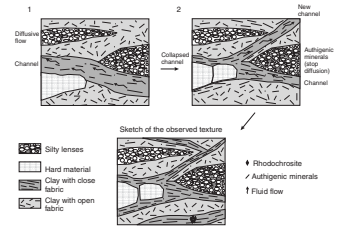
F15. General morphology of spaced foliation, p. 32.
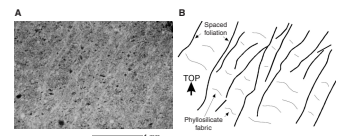
The lower chalk unit displayed notably high permeabilities, even given the extremely indurated nature of the sediment. Figure F11 indicates that both the initial permeability and postshear permeability are of similar values, even though axial deformation resulted in discrete faults that bore a close resemblance to the normal faults seen in section. It seems unlikely that faulting within Unit U3 would impact significantly on bulk dewatering.

CONCLUSIONS

Detailed mesoscopic and microscopic analyses of the two lower slope sites drilled in the Costa Rica subduction complex have revealed three distinct structural/hydrological regimes. The sedimentary prism records fluctuations in the maximum principal stress from vertical to near horizontal because of variations in the fluid pressure. Earlier structures, such as kink bands and vertical deformation bands, result primarily as accommodation structures in response to progressive burial. Superimposed on these structures are bedding-parallel deformation bands, interpreted as shear bands that formed by rotation of the principal stress and subsequent shear compaction. They display intensely aligned clay particles arising from porosity collapse, fabrics that result in a bulk decrease in permeability that do not focus fluids extensively.

The décollement zone is characterized by heterogeneous grain-size distribution, deformation style, and clay mineral fabric. Diffusive flow occurs in more silty zones, with more focused flow along brittle fracture surfaces. Experimental data confirm that permeability can vary along such fractures in response to fluid pressure. The bulk flow pattern along the décollement is interpreted here to represent prolonged periods of fluid pressure buildup interspersed with short-lived, transient episodes of enhanced fluid flow as fractures interconnect and allow dissipation of pressurized fluids. Both the hydrological and structural features point to shear failure under conditions of either reduced effective stress due to raised fluid pressure after consolidation or within regions where incipient cementation has provided enough internal strength to allow strain softening and localized slip to occur.

The underthrust unit displays markedly different deformational style from both the prism and décollement, indicative of efficient decoupling between the two plates, as observed for other margins (e.g., Barbados; Housen et al., 1996). Comparison of physical properties profiles between the underthrust sections and the reference site show that much of the compactional thinning of individual units occurs through porosity loss alone. However, the presence of bedding-parallel deformation bands and normal faults suggests that strain has become localized in certain regions but are unlikely to affect dewatering processes.

The results have implications for other convergent margins that, while containing lithologically distinct sediments, exhibit similar patterns of focused flow and geochemical anomalies, for example, Barbados (Moore, Klaus, et al., 1998); Nankai (Taira, Hill, Firth, et al., 1991); and Cascadia (Westbrook, Carson, Musgrave, et al., 1994). Fault zones need not have intrinsically higher matrix permeabilities than surrounding sediment. Indeed, fracture-induced flow is more likely to occur in sediments that are extremely overconsolidated and hence more susceptible to brittle failure. The accompanying response may be a drop in fluid pressure, implying that overpressure is not a prerequisite for dilation and development of a fracture permeability.

ACKNOWLEDGMENTS

REFERENCES

Bangs, N.L.B., Westbrook, G.K., Ladd, J.W., and Buhl, P., 1990. Seismic velocities from the Barbados Ridge Complex: indicators of high pore fluid pressures in an accretionary complex. *J. Geophys. Res.,* 95:8767–8782.

Behrmann, J.H., Lewis, S.D., Musgrave, R.J., et al., 1992. *Proc. ODP, Init. Repts.,* 141: College Station, TX (Ocean Drilling Program).

Bekins, B.A., McCaffrey, A.M., and Driess, S.J., 1995. Episodic and constant flow models for the origin of low-chloride waters in a modern accretionary complex. *Water Resour. Res.,* 31:3205–3215.

Bolton, A.J., Clennell, M.B., and Maltman, A.J., 1999. Non-linear stress dependency of permeability: a mechanism for episodic fluid flow in accretionary wedges. *Geology*, 27:239–242.

Bolton, A.J., Maltman, A.J., and Clennell, M.B., 1998. The importance of overpressure timing and permeability evolution in fine-grained sediments undergoing shear. *J. Struct. Geol.,* 20:1013–1022.

Borradaile, G.J., Bayly, M.B., and Powell, C.M., 1982. *Atlas of Deformational and Metamorphic Rock Fabric:* Berlin (Springer-Verlag).

Bray, C.J., and Karig, D.E., 1985. Porosity of sediments in accretionary prisms and some implications for dewatering processes. *J. Geophys. Res.,* 90:768–778.

Brothers, R.J., Kemp, A.E.S., and Maltman, A.J., 1996. Mechanical development of vein structures due to the passage of earthquake waves through poorly consolidated sediments. *Tectonophysics,* 260:227–244.

Brown, K.M., 1995. The variation of the hydraulic conductivity structure of an overpressured thrust zone with effective stress. *In* Carson, B., Westbrook, G.K., Musgrave, R.J., and Suess, E. (Eds.), *Proc. ODP, Sci. Results,* 146 (Pt 1): College Station, TX (Ocean Drilling Program), 281–289.

Brown, K.M., Bekins, B., Clennell, B., Dewhurst, D., and Westbrook, G., 1994. Heterogeneous hydrofracture development and accretionary fault dynamics. *Geology,* 22:259–262.

Byrne, T., Maltman, A., Stephenson, E., Soh, W., and Knipe, R., 1993. Deformation structures and fluid flow in the toe region of the Nankai accretionary prism. *In* Hill, I.A., Taira, A., Firth, J.V., et al., *Proc. ODP, Sci. Results,* 131: College Station, TX (Ocean Drilling Program), 83–101.

Carson, B., and Screaton, E.J., 1998. Fluid flow in accretionary prisms: evidence for focussed, time-variable discharge. *Rev. Geophys.,* 36:329–351.

Demets, C., Gordon, R.G., Argus, D.F., and Stein, S., 1990. Current plate motions. *Geophys. J. Int.,* 101:425–478.

Fisher, A.T., Zwart, G., and Shipboard Scientific Party, 1996. The relationship between permeability and effective stress along a plate-boundary fault, Barbados accretionary complex. *Geology,* 24:307–310.

Housen, B.A., and the ODP Leg 156 Scientific Party, 1996. Strain decoupling across the décollement of the Barbados accretionary prism. *Geology,* 24:127–130.

Hubbert, M.K., and Rubey, W.W., 1959. Role of fluid pressures in mechanics of overthrust faulting, Part 1. Mechanics of fluid-filled porous solids and its application to overthrust faulting. *Geol. Soc. Am. Bull.,* 70:115–166.

Karig, D.E., 1990. Experimental and observational constraints on the mechanical behavior in the toes of accretionary prisms. *In* Knipe, R.J., and Rutter, E.H. (Eds.), *Deformation Mechanisms, Rheology, and Tectonics.* Geol. Soc. Spec. Publ. London, 54:383–398.

Kastner, M., Elderfield, H., and Martin, J.B., 1991. Fluids in convergent margins: what do we know about their composition, origin, role in diagenesis and importance for oceanic chemical fluxes? *Philos. Trans. R. Soc. London A,* 335:243–259.

Kimura, G., Silver, E.A., Blum, P., et al., 1997. *Proc. ODP, Init. Repts.,* 170: College Station, TX (Ocean Drilling Program).

Labaume, P., Maltman, A.J., Bolton, A., Tessier, D., Ogawa, Y., and Takizawa, S., 1997. Scaly fabrics in sheared clays from the décollement zone of the Barbados accretionary prism. *In* Shipley, T.H., Ogawa, Y., Blum, P., and Bahr, J.M. (Eds.), *Proc. ODP, Sci. Results,* 156: College Station, TX (Ocean Drilling Program), 59–77.

Maltman, A.J., 1998. Deformation structures from the toes of accretionary prisms. *J. Geol. Soc. London,* 155:639–650.

Mascle, A., Moore, J.C., et al., 1988. *Proc. ODP, Init. Repts.,* 110: College Station, TX (Ocean Drilling Program).

Moore, J.C., Klaus, A., et al., 1998. *Proc. ODP, Init. Repts.,* 171A: College Station, TX (Ocean Drilling Program).

Moore, J.C., and the ODP Leg 156 Scientific Party, 1995. Abnormal fluid pressures and fault zone dilation in the Barbados accretionary prism: evidence from logging while drilling. *Geology,* 23:605–608.

Olson, R.E., and Daniel, D.E., 1981. Measurement of the hydraulic conductivity of fine-grained soils. *In* Zimmie, T.F., and Riggs, C.O. (Eds.), *Permeability and Groundwater Contaminant Transport.* ASTM Spec. Tech. Publ., 746:18–64.

Screaton, E.J., Fisher, A.T., Carson, B., and Becker, K., 1995. Hydrogeological properties of a thrust fault within the Oregon accretionary prism. *J. Geophys Res.,* 95:8997–9007.

————, 1997. Barbados Ridge hydrogeologic tests: implications for fluid migration along an active décollement. *Geology,* 25:239–242.

Shipley, T.H., Ogawa, Y., Blum, P., et al., 1995. *Proc. ODP, Init. Repts.,* 156: College Station, TX (Ocean Drilling Program).

Skempton, A.W., 1966. Some observations of tectonic shear zones. *Proc. 1st Int. Conf. Rock Mech.,* 6:329–335.

Stephenson, E.L., Maltman, A.J., and Knipe, R.J., 1994. Fluid flow in actively deforming sediments: 'dynamic permeability' in accretionary prisms. *In* Parnell, J. (Ed.), *Geofluids: Origin, Migration and Evolution of Fluids in Sedimentary Basins.* Geol. Soc. London Spec. Publ. London, 78:113–125.

Suppe, J., 1985. *Principles of Structural Geology:* Englewood Cliffs, NJ (Prentice-Hall).

Taira, A., Hill, I., Firth, J.V., et al., 1991. *Proc. ODP, Init. Repts.,* 131: College Station, TX (Ocean Drilling Program).

Westbrook, G.K., Carson, B., Musgrave, R.J., et al., 1994. *Proc. ODP, Init. Repts.,* 146 (Pt. 1): College Station, TX (Ocean Drilling Program).

Zwart, G., Brückmann, W., Moran, K., MacKillop, A.K., Maltman, A.J., Bolton, A., Vrolijk, P., Miller, T., Gooch, M.J., and Fisher, A., 1997. Evaluation of hydrogeologic properties of the Barbados accretionary prism: a synthesis of Leg 156 results. *In* Shipley, T.H., Ogawa, Y., Blum, P., and Bahr, J.M. (Eds.), *Proc. ODP, Sci. Results,* 156: College Station, TX (Ocean Drilling Program), 303–310.

Figure F1. Location map offshore Costa Rica, indicating the five sites drilled during Leg 170.
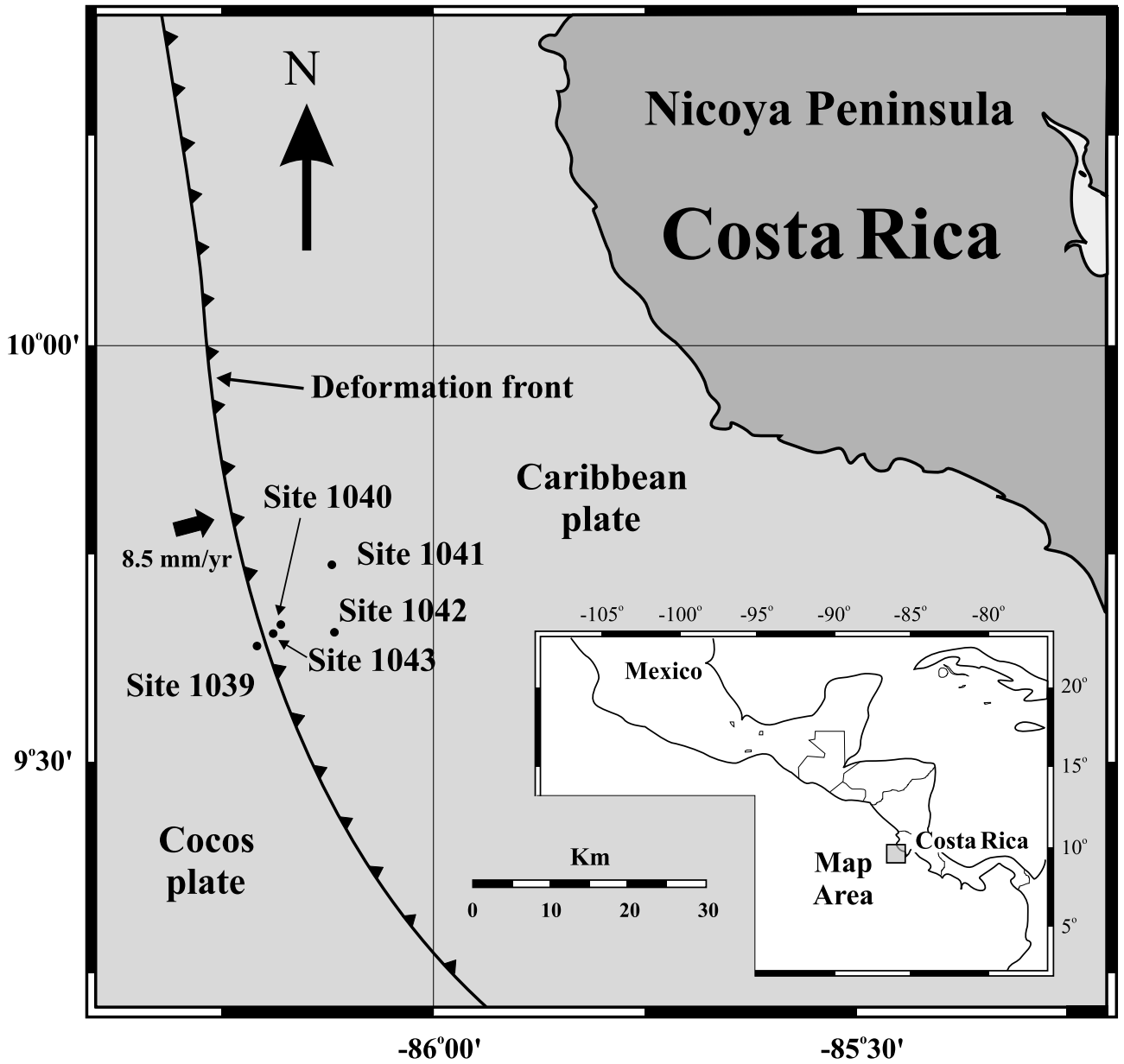
Figure F2. Diagram showing the experimental setup for permeability/geotechnical analysis. Samples are placed in a triaxial cell and subjected to a range of confining and fluid pressures, with associated volumetric and permeability variations measured, both during uniaxial and triaxial deformation. See text for further details. DPT = differential pressure transducer and DT = displacement transducer.
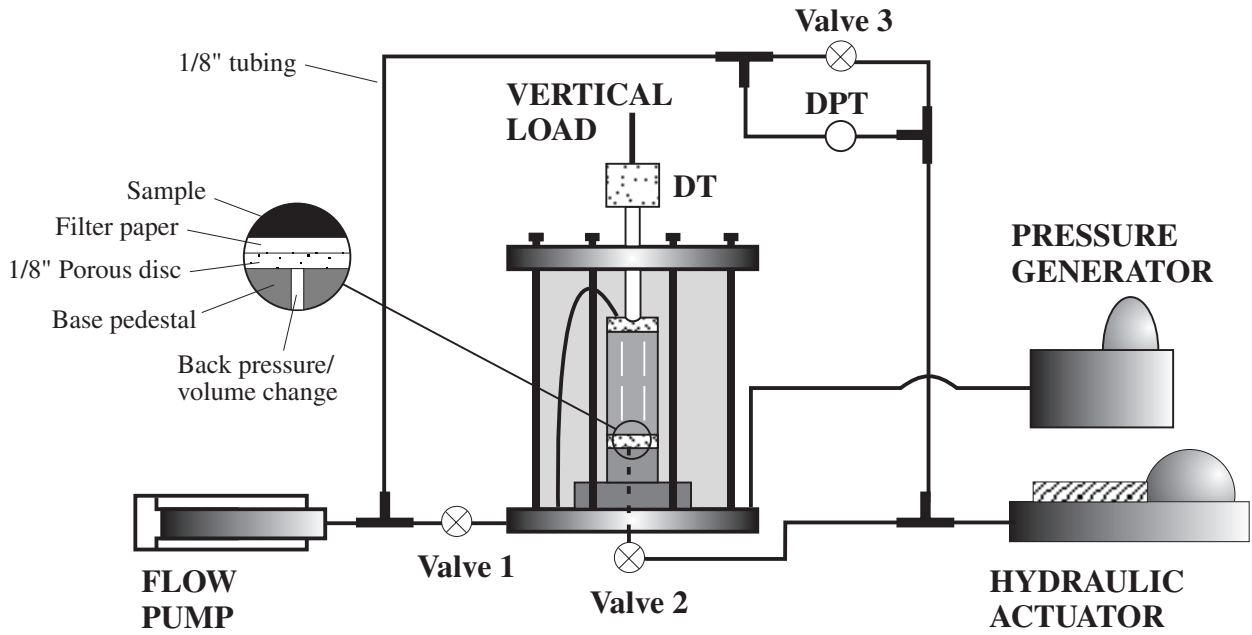
Figure F3. Generalized stratigraphic column observed at the reference site (Site 1039) and the two prism sites located at the toe of the deformed sedimentary wedge (Sites 1040 and 1043).
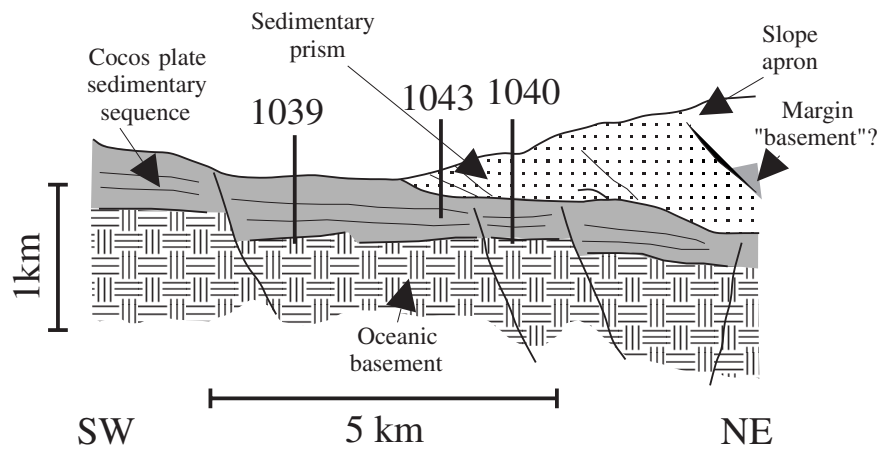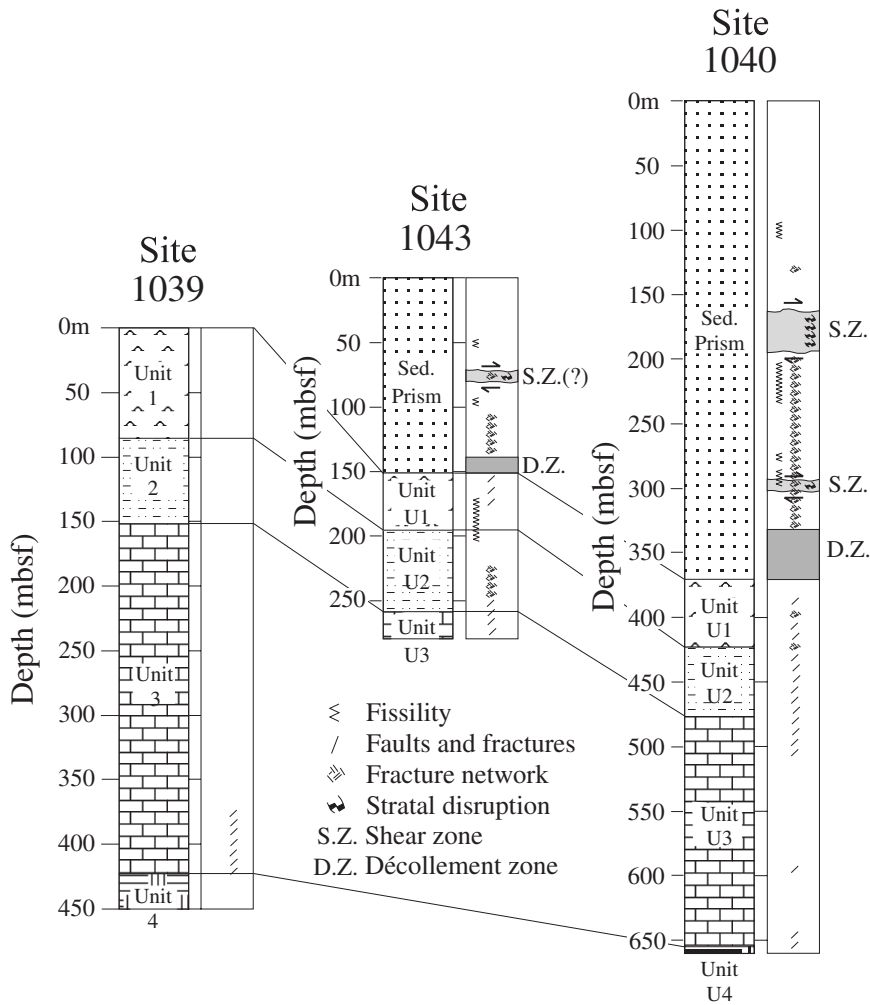
Figure F4. A. Secondary electron micrograph showing the general morphology of kink bands, observed only in certain horizons below 150 mbsf. **B.** Diagram highlighting the relevant features.

A
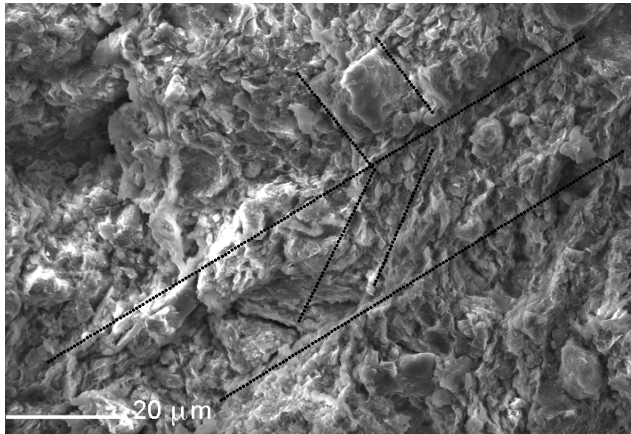
B
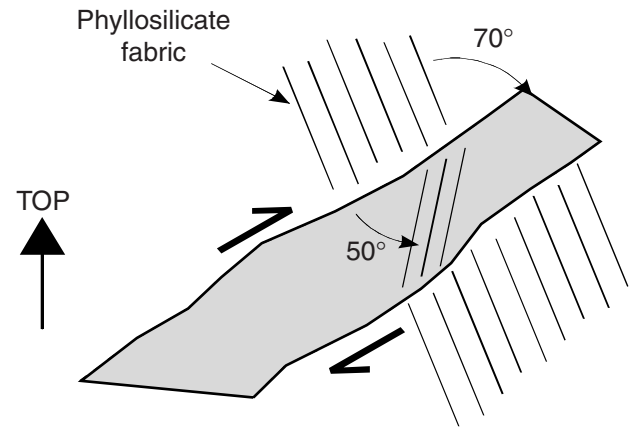
Figure F5. General morphology of deformation bands. **A.** Optical micrograph illustrating the discrete nature of individual slip bands. **B.** Secondary electron micrograph showing intense grain alignment at the shear zone boundary. **C.** Optical micrograph of a more broadly defined deformation band, showing domains of variously intensely aligned phyllosilicates. **D.** Diagram illustrating the various interrelationships.

A
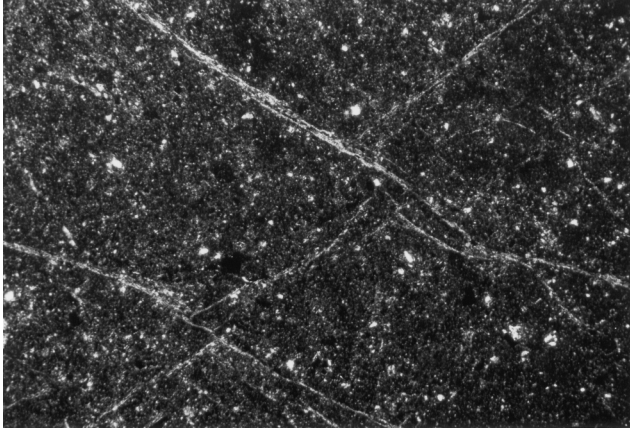
B
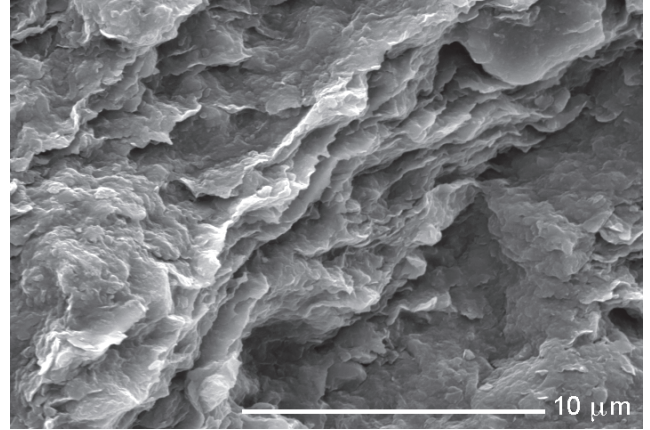
C
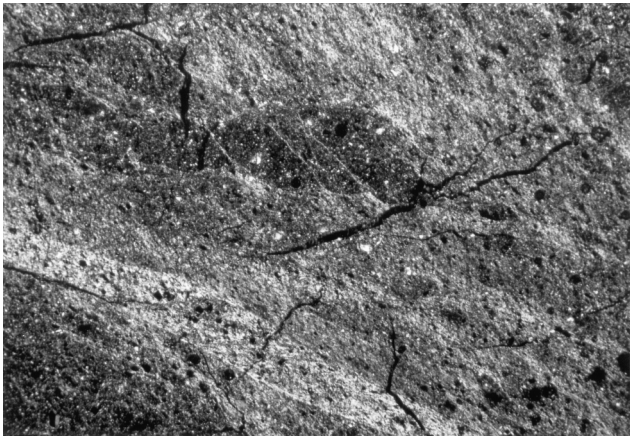
D
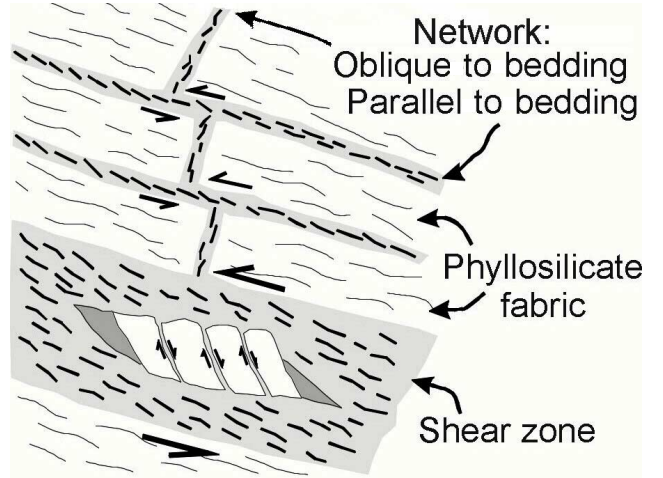
Figure F6. A. Photomicrograph showing a burrow being displaced by an array of discrete, steeply inclined faults. **B.** Diagram highlighting relevant features.

A

1 mm

B

Phyllosilicate fabric

Faults

Burrow
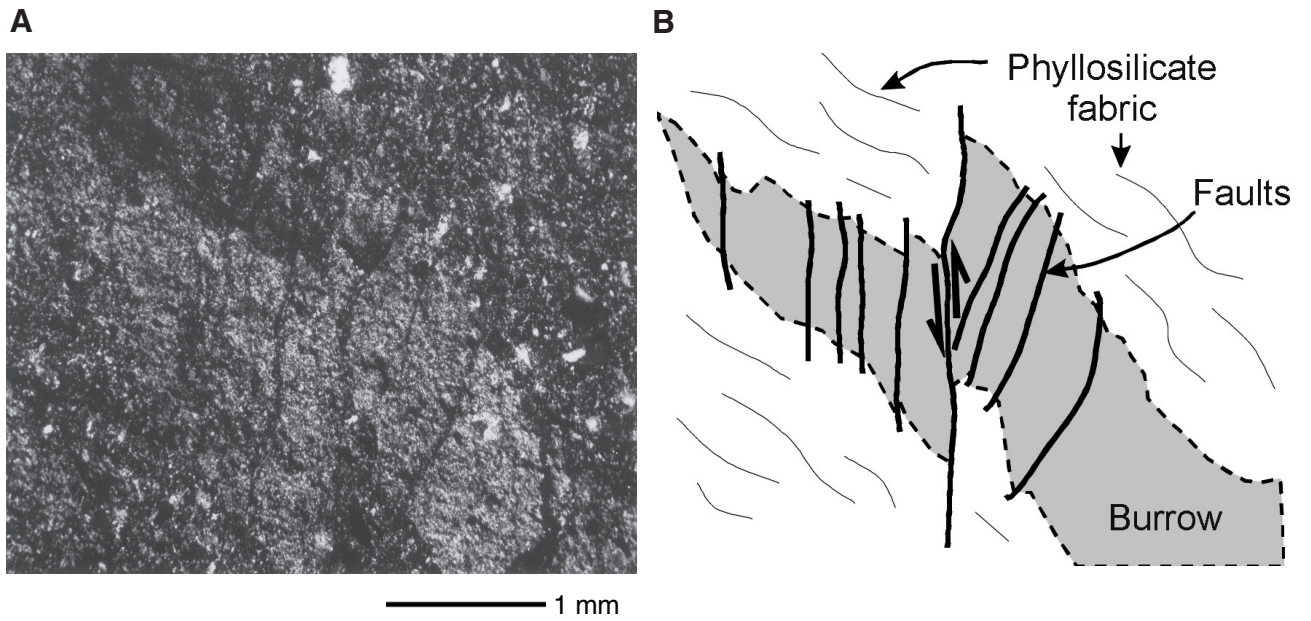
Figure F7. A. Core photograph depicting the entire décollement interval. Note the transition from blocky, lenticular fragments in the upper half to plastic, drilling-disturbed mud in the lower section. (Continued on next page.)

Figure F7 (continued). B. Detailed structural column through the décollement highlighting the main features shown in Figure F7A, p. 22.
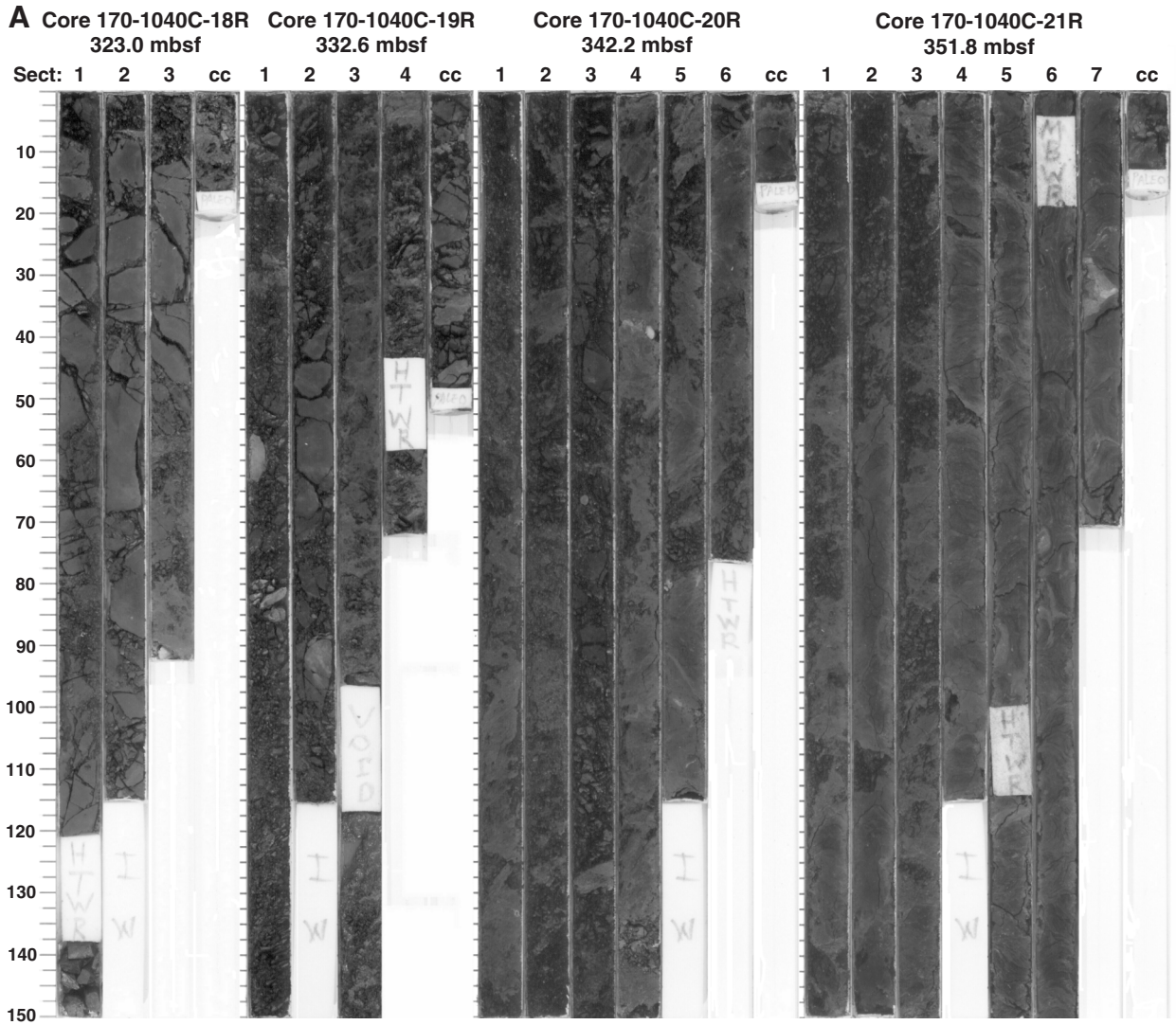
Figure F8. Sequence of secondary electron micrographs, showing relevant features of the décollement. **A.** Fracture arrays in the upper part dividing the material into blocky fragments. **B.** Undeformed clays in between fractures. **C.** Draping of clay minerals around siltier grains. **D.** Fracture surfaces, localizing in clay-rich domains. **E.** Looking flat on to a shear surface. Note the planar nature and intense grain alignment.

A
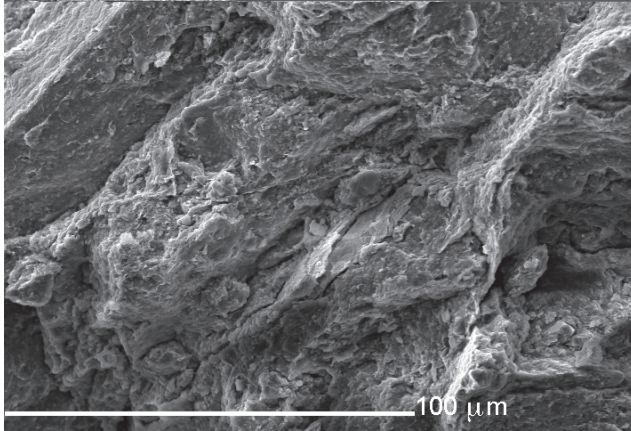
B
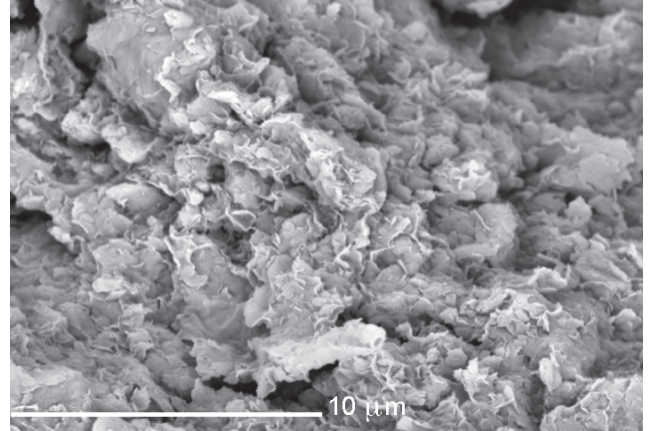
C
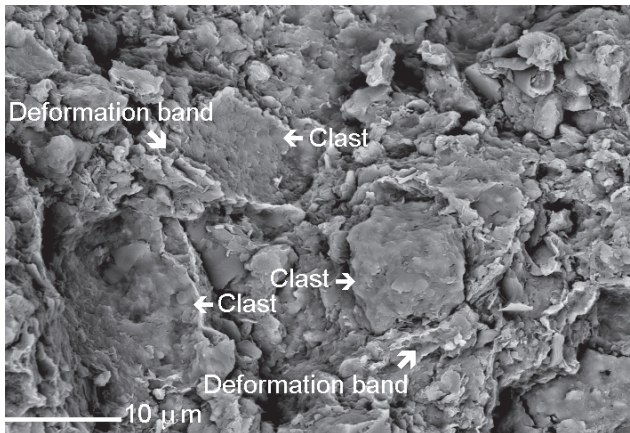
D
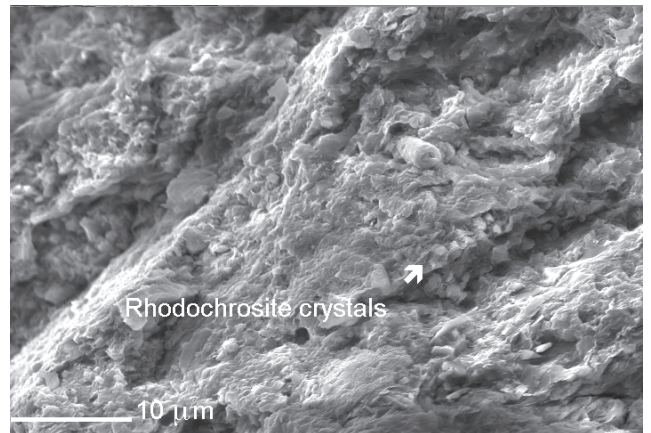
E
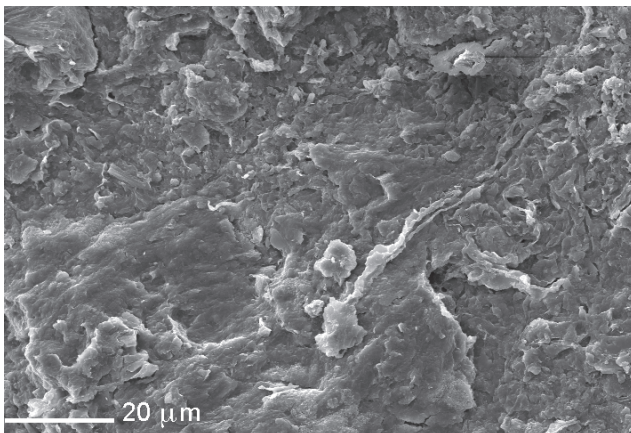
Figure F9. Evidence for recrystallization within the underthrust section. **A.** Secondary SEM image of a recrystallized microfossil with neomorphic calcite and quartz needles (Site 1040, 411.70 mbsf). **B.** Backscattered SEM image of a nonrecrystallized radiolarian with intact spines (Site 1040, 421.62 mbsf).

A

20 μm

B
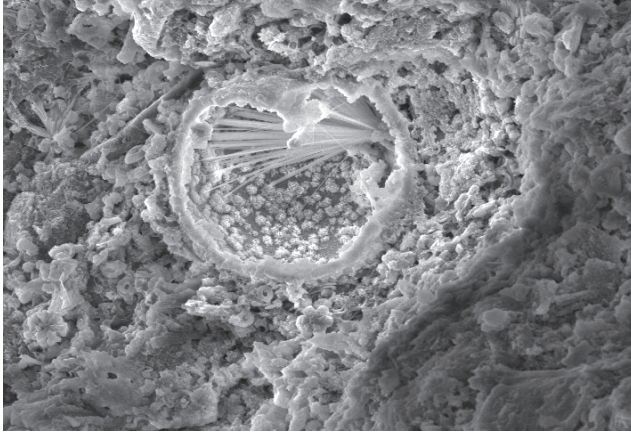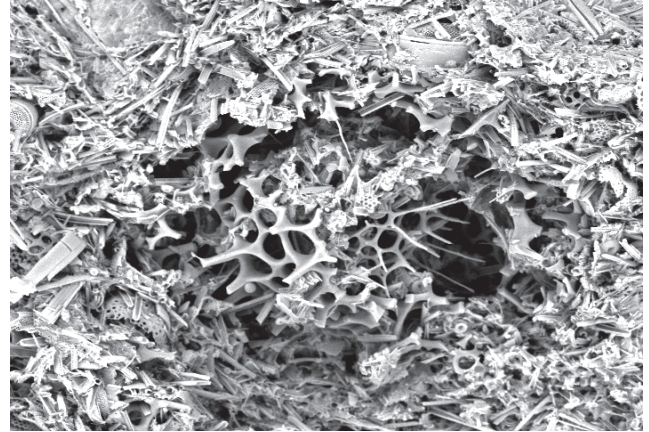
20 μm

Figure F10. A. Permeability vs. effective stress relationships of whole-round samples tested prior to axial loading. **B.** Porosity vs. effective stress relationship for the same samples. (Note the linear relationship in all cases).
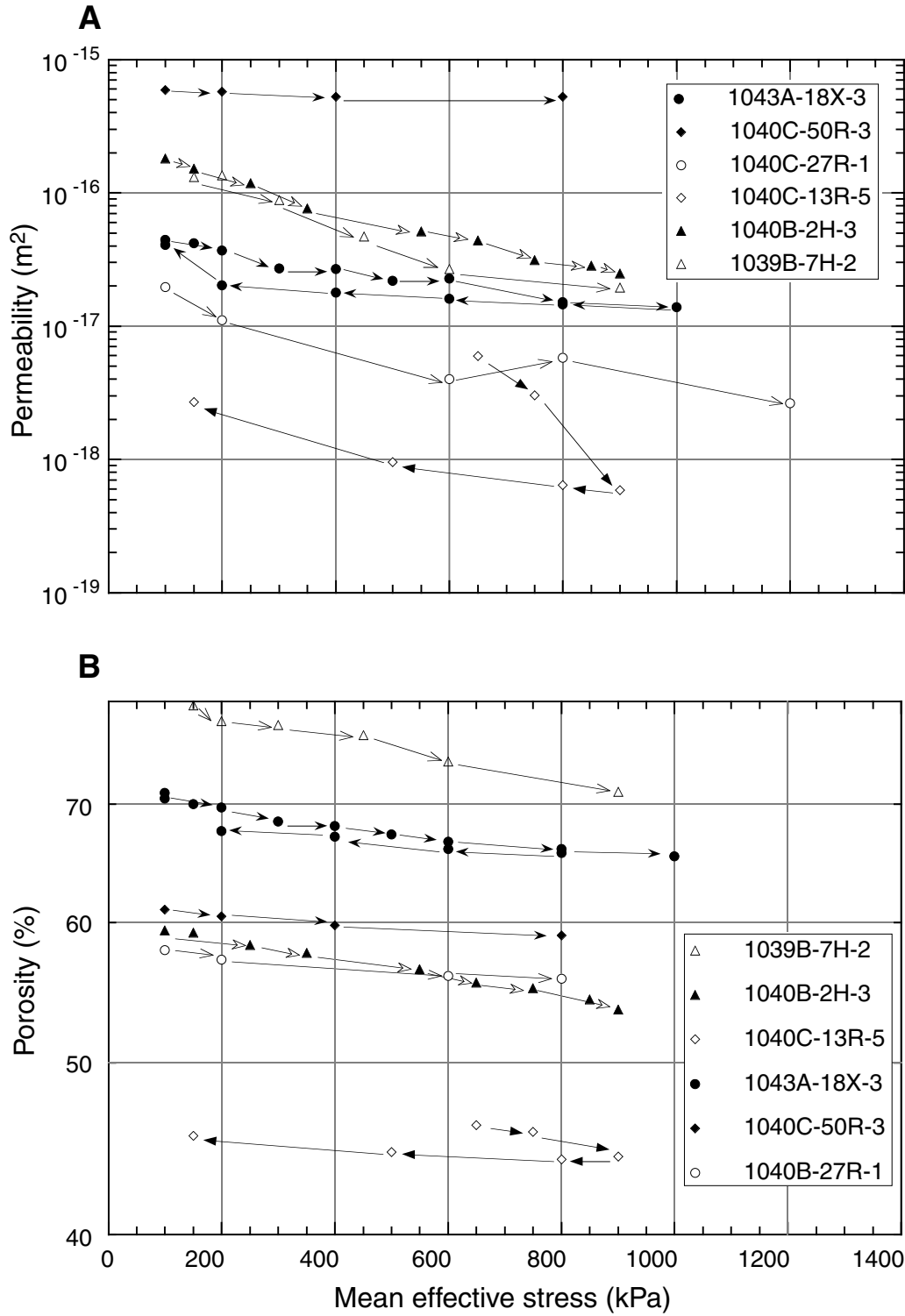
Figure F11. Summary of permeability vs. effective stress relationships both before and after shear. Individual data points connect maximum and minimum values of permeability before and after shear. In all cases bar one (Sample 170-1040C-13R-5, 88–105 cm) changes in permeability are no greater than one order of magnitude.
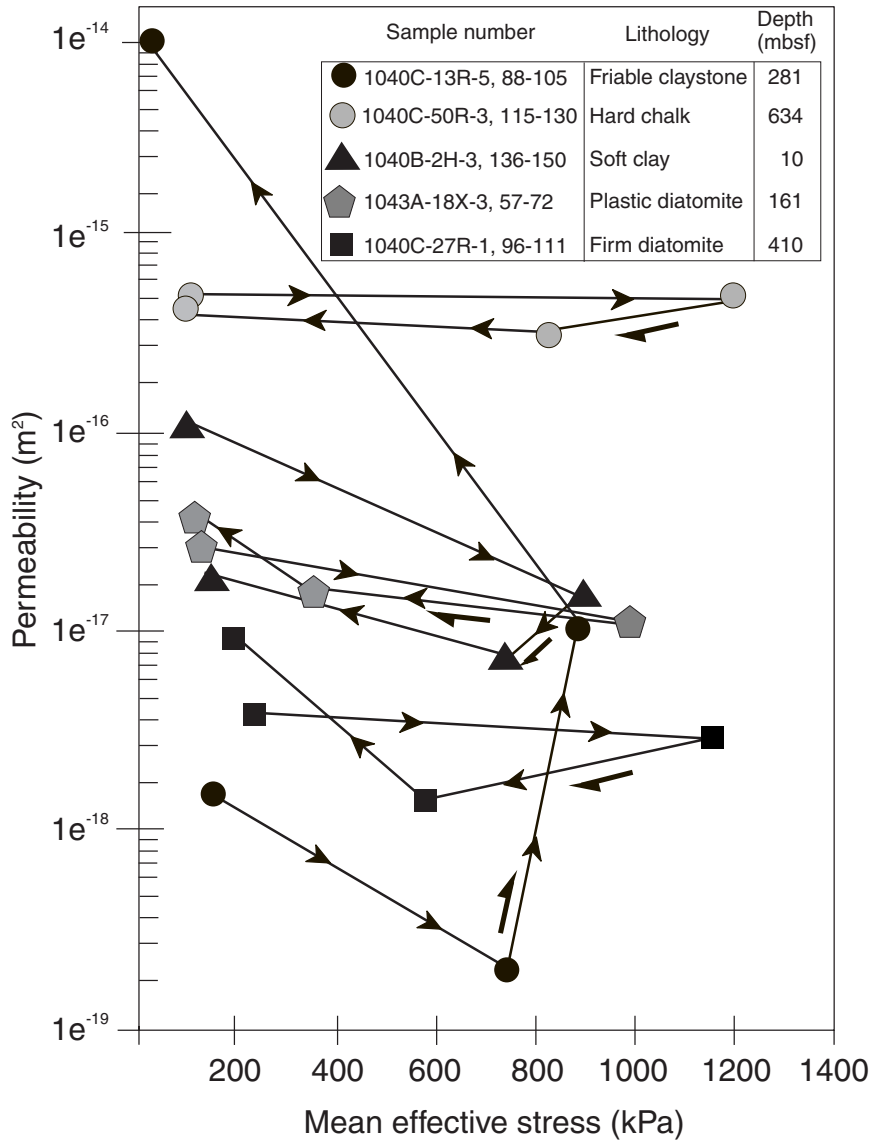
Figure F12. A. Differential fluid pressure (the fluid pressure difference between the ends of the sample) vs. time during undrained shear of friable claystone (Sample 170-1040C-13R-5, 88–105 cm). Note the fluid pressure increases initially (indicative of contractive deformation) followed by larger drop-offs in fluid pressure, associated with fluid drawn into a dilating shear zone. **B.** Porosity vs. permeability before and after shear of the same sample. Note how after deformation, smaller changes in porosity yield larger changes in permeability (seen as a flattening of the relative curves). (Continued on next page.)
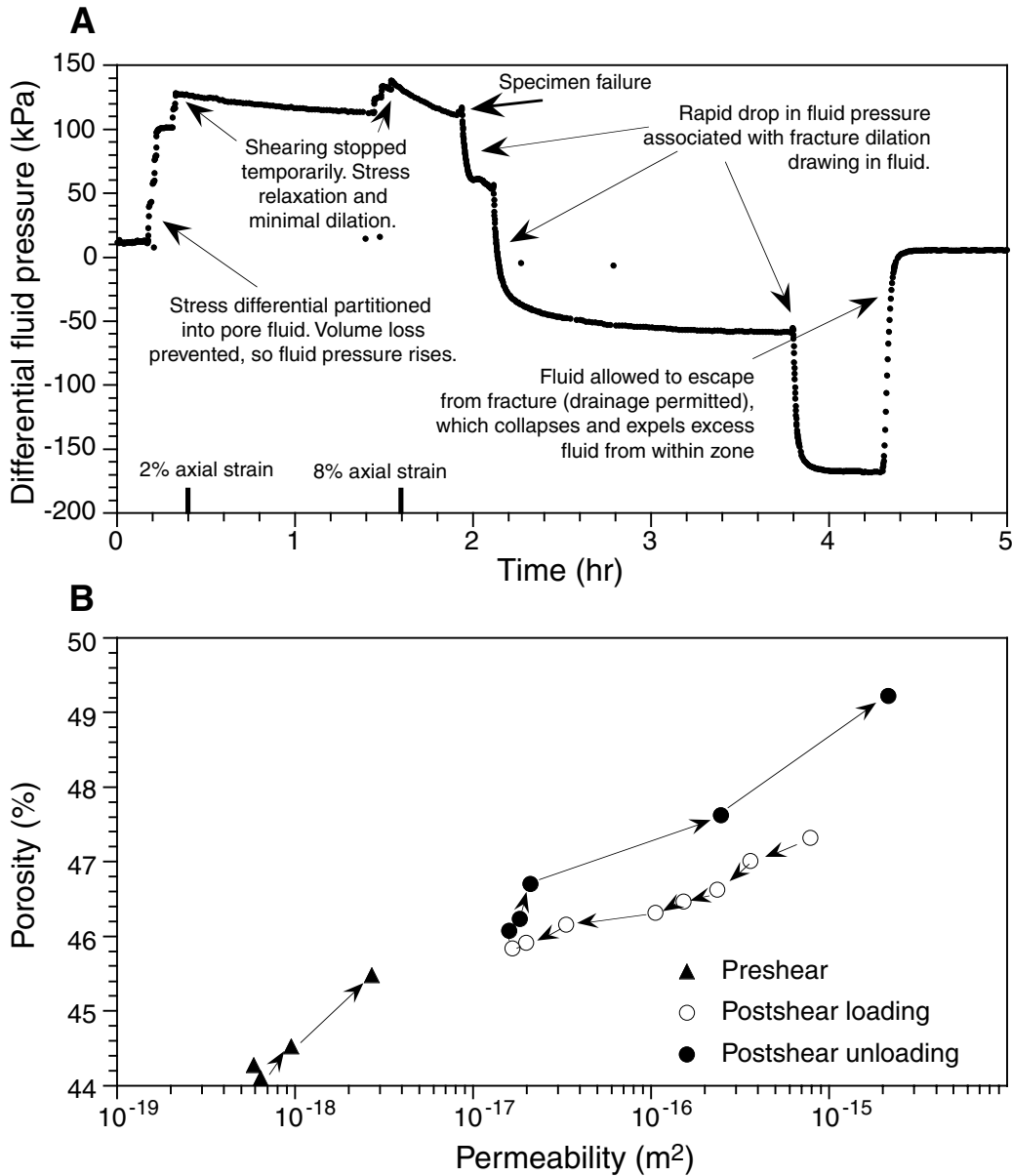
Figure F12 (continued). C. Permeability vs. effective stress both before and after shear. First permeability test after deformation was conducted after reduction of the confining pressure to 100 kPa effective stress (marked on the graph). At the lowest values of effective stress after deformation, permeability is more than three orders of magnitude greater than before deformation.
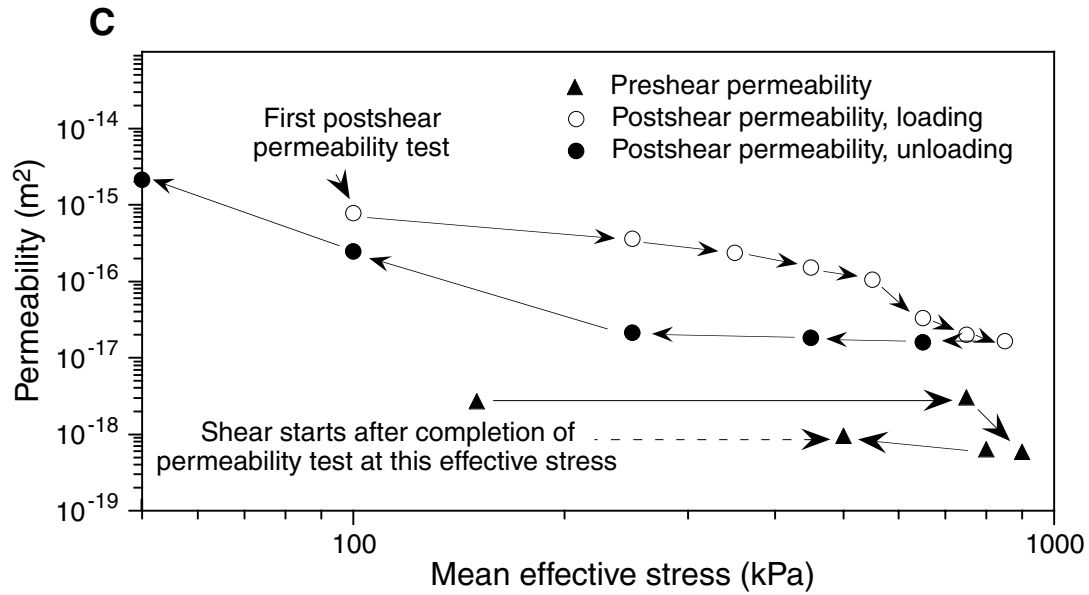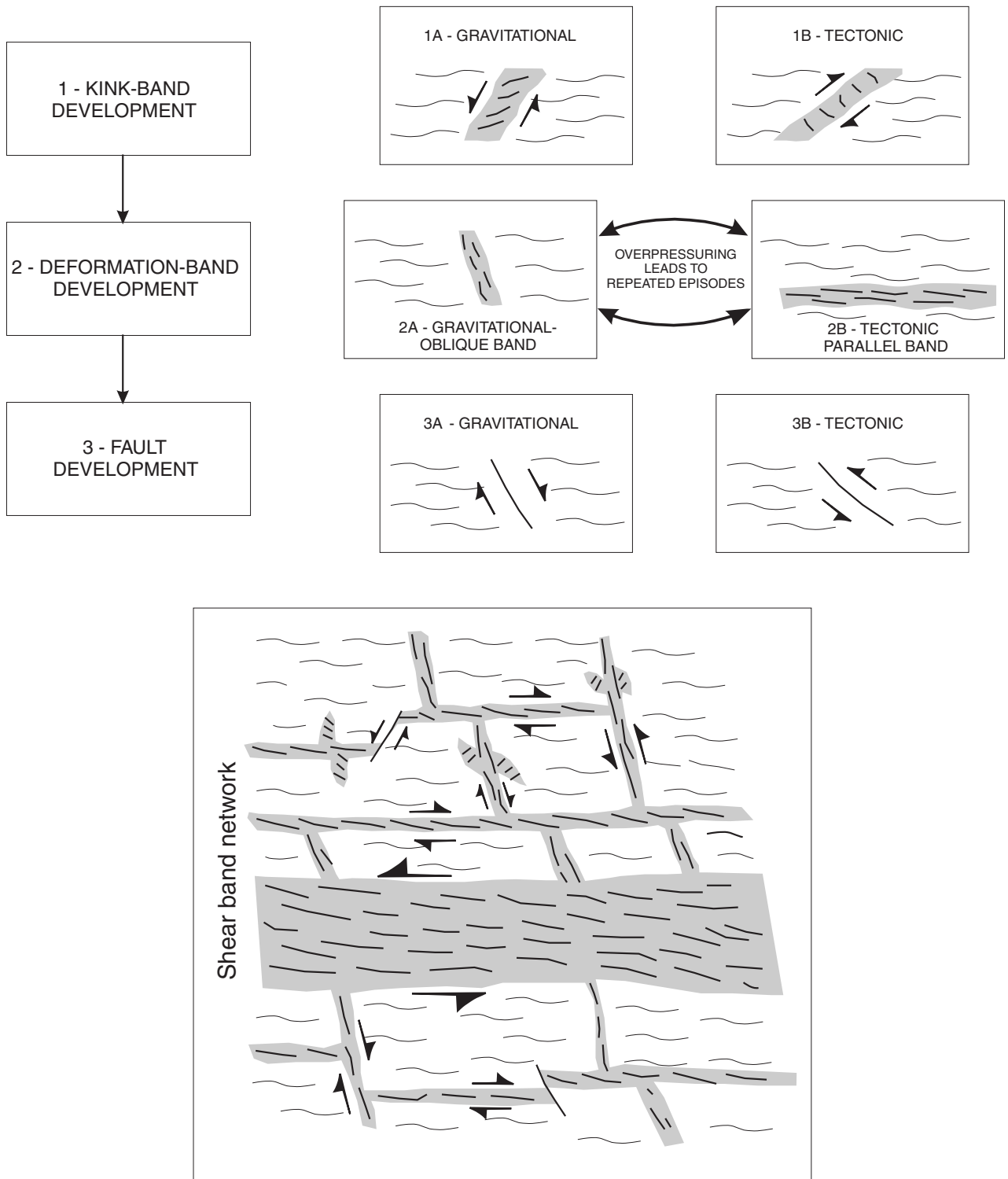
Figure F13. Illustration showing the sequential development of kink bands and deformation bands and how they interrelate.

Figure F14. Summary of the different microstructures observed within the décollement, indicative of heterogeneous fluid flow regimes. See text for discussion.
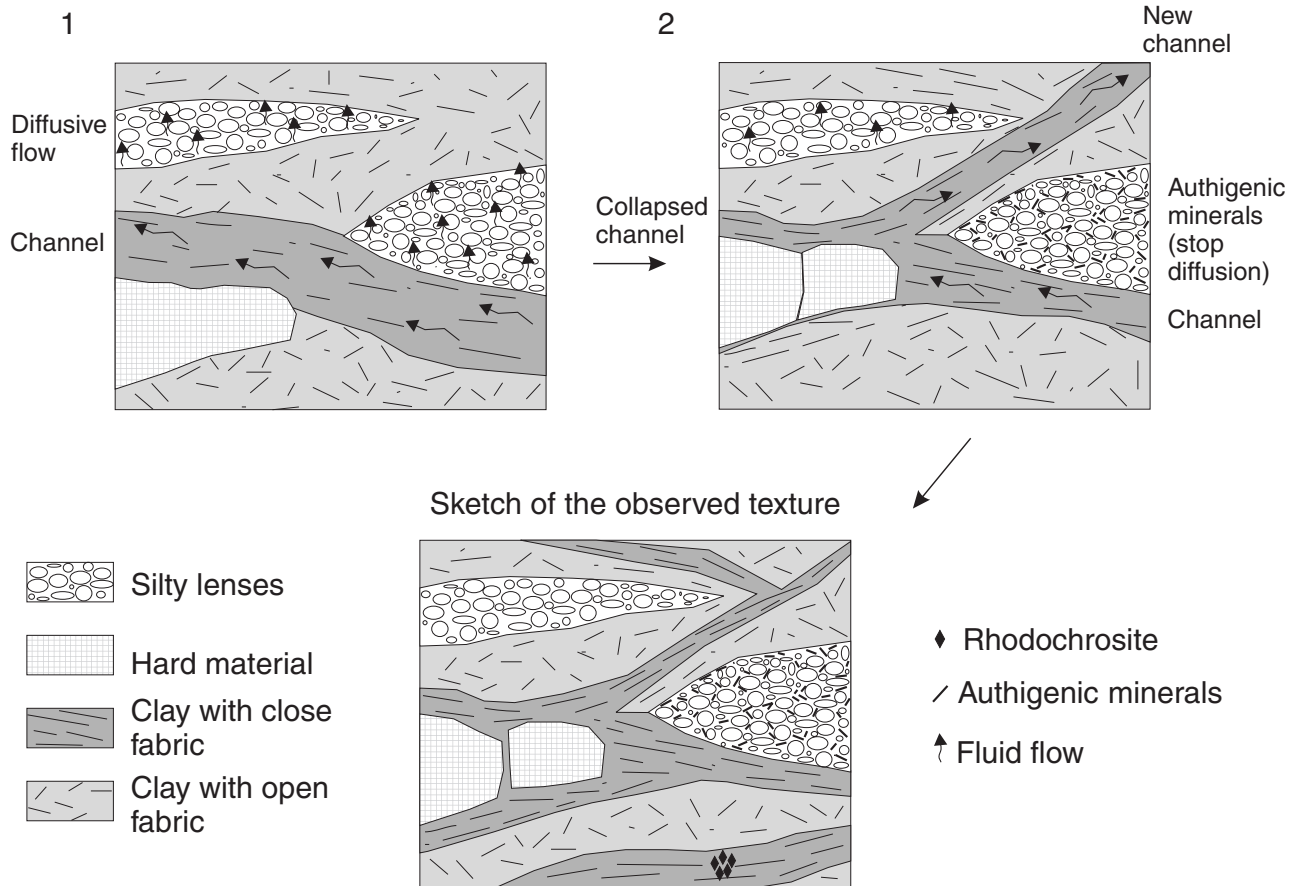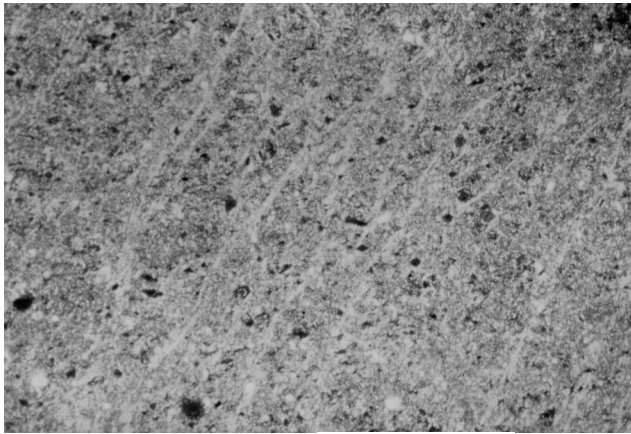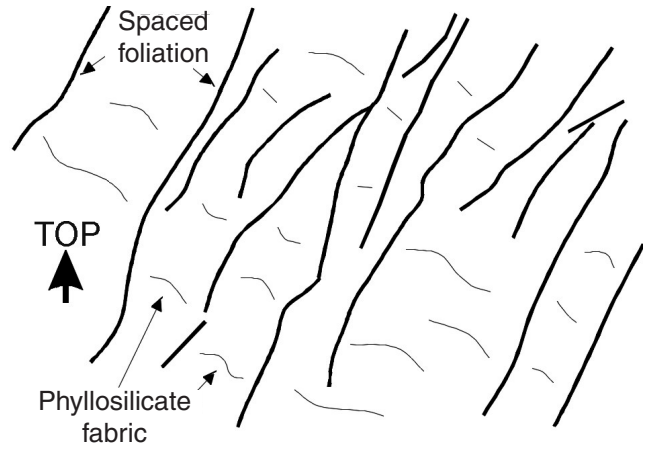
Figure F15. A. Optical micrograph showing the general morphology of spaced foliation. **B.** Diagram highlighting relevant features.